

HGT: A Hierarchical GCN-Based Transformer for Multimodal Periprosthetic Joint Infection Diagnosis Using CT Images and Text

Ruiyang Li¹, Fujun Yang², Xianjie Liu² and Hongwei Shi^{2,*}

¹ Sichuan University, College of Electronics and Information Engineering, Chengdu, Sichuan, China

² Sichuan University, College of Computer Science, Chengdu, Sichuan, China

* Correspondence: shihw001@126.com

Abstract: Prosthetic Joint Infection (PJI) is a prevalent and severe complication characterized by high diagnostic challenges. Currently, a unified diagnostic standard incorporating both computed tomography (CT) images and numerical text data for PJI remains unestablished, owing to the substantial noise in CT images and the disparity in data volume between CT images and text data. This study introduces a diagnostic method, HGT, based on deep learning and multimodal techniques. It effectively merges features from CT scan images and patients' numerical text data via a Unidirectional Selective Attention (USA) mechanism and a graph convolutional network (GCN)-based feature fusion network. We evaluated the proposed method on a custom-built multimodal PJI dataset, assessing its performance through ablation experiments and interpretability evaluations. Our method achieved an accuracy (ACC) of 91.4% and an area under the curve (AUC) of 95.9%, outperforming recent multimodal approaches by 2.9% in ACC and 2.2% in AUC, with a parameter count of only 68M. Notably, the interpretability results highlighted our model's strong focus and localization capabilities at lesion sites. This proposed method could provide clinicians with additional diagnostic tools to enhance accuracy and efficiency in clinical practice.

Keywords: Prosthetic Joint Infection (PJI), Deep Learning Diagnosis, Multimodal Fusion, CT imaging, Graph Convolutional Neural Networks (GCNs), Unidirectional Selective Attention (USA)

1. Introduction

Periprosthetic joint infection (PJI) is a catastrophic complication that may arise following joint replacement surgery. The diagnosis of prosthetic joint infections (PJI) poses a significant challenge since real evidence-based guidelines to aid clinicians in choosing the most accurate diagnostic strategy are lacking. The Musculoskeletal Infection Society (MSIS) criteria for PJI, proposed by the Second International Consensus Meeting (ICM) in 2018 offers an evidence-based definition for diagnosing hip and knee PJI [1], which presents a scoring approach to diagnosis based on the most robust evidences. However, this criteria is based on clinical performance and biochemical test results, particularly the serological, synovial, and microbiological tests, keeping its complexity in the clinical use.

Infact, most signs and symptoms that might indicate the presence of a PJI may be simply related to an aseptic loosening of the prosthesis or to a soft tissue infection [2]. Radiographical examinations are widely used to detect the cause of the stmptons. Among various radiographical examinations, X-ray examination take the first place for the evaluation of possibly infacted cases, while computed tomography (CT) findings are rarely utilized as a diagnostic basis [3]. In the radiological perspective, CT scans contain more invisible radiologic signs than X-ray, which achieves its significant potential value for PJI diagnosis [4]. As computer vision technology advances, deep learning techniques can be now employed to utilize imaging findings for PJI diagnosis, extracting features from invisible sites within the information-rich CT scans. Among the numerous image processing networks,transformer-based architectures exhibit exceptional texture extraction capabilities, rendering them suitable for PJI diagnosis based on CT images. Nevertheless, traditional transformer based structures struggle to aggregate information from multiple

images (generated by single CT-scan), and the immense computational cost arising from the large number of images is unacceptable. As a result, there is a pressing need for a method that can effectively aggregate information from numerous CT images.

Joint evaluation of Radiological and biochemical examination results can maximize the accuracy of PJI diagnosis; however, a unified diagnostic standard for PJI is yet to be established. As a solution, Multimodal techniques can integrate imaging findings with patient text data (serological markers, medical history, e.g.). There are five main challenges in the research field of Multimodal Machine Learning: (1) **Representation** Learning how to represent and summarize multimodal data in a way that exploits the complementarity and redundancy of multiple modalities. (2) **Translation** Learning to translate data from one modality to another. (3) **Alignment** Learning to identify the direct relations between (sub)elements from two or more different modalities. (4) **Fusion** Learning to join information from two or more modalities to perform a prediction. (5) **Co-learning** Learning to transfer knowledge between modalities, their representation, and their predictive models [5]. From these challenges above, PJI Diagnosis can be considered as a Modality Fusion challenge.

Deep integration of image and text modalities is the key to improve PJI diagnosis accuracy. Recent multimodel neural networks, such as ViLT [6], ViLBERT [7], and IMAGE-BERT [8], UniT [9], typically manage modality fusion between text in sentences and image information. For PJI Diagnosis, patient text features consist of single numerical vectors that are considerably smaller in data volume compared to images. And due to the substantial noise in CT images, the numerical vectorized text features might show a greater correlation with PJI. Consequently, The difficulty of employing recent multimodel neural networks for PJI diagnosis arises from two main problems: (1) overfitting of text data, and (2) excessive reliance on text data, neglecting feature extraction from images. To better utilize image data as well as mitigate the network's bias towards text data, it is crucial to minimize the impact of extensive noise within CT images and prevent the overfitting of text data.

To address these challenges, we proposed a novel network structure, named as HGT in this study, which is a 5-stage Modality fusion network based on Transformer Architecture. Three main innovation of the architecture can be elaborated in three main aspects: (1) Before all stages, **A Image Sampling Strategy** is proposed to reduce computational complexity by sampling the CT images derived from single-scan before the whole modality fusion process. (2) In the 1st to 4th stage of HGT, a **Unidirectional Selective Attention (USA)** is used for deep fusion between image features and text feature. (3) At the final stage of the network, a **Feature Fusion network based on graph convolutional neural networks (GCNs)** [10] is proposed to fuse features between different CT images. In more detail, the Unidirectional Selective Attention (USA) enables text data to selectively attend to important features within high-noise CT image data for modality fusion. The proposed Feature Fusion network integrates features by reducing the graph complexity through a coarsening process. For this process, we develop a feature selective algorithm to sample lesion site features among all input CT images. By evaluating on self-created PJI dataset, HGT achieves state-of-the-art performance. The network structure is shown in Figure 1.

This network effectively utilizes both the numerical text data of patients and CT image features for PJI diagnosis. It substantially enhances clinical diagnostic efficiency and reduces PJI misdiagnosis rates, which has significant clinical implications for the prevention and treatment of secondary occurrence of PJI.

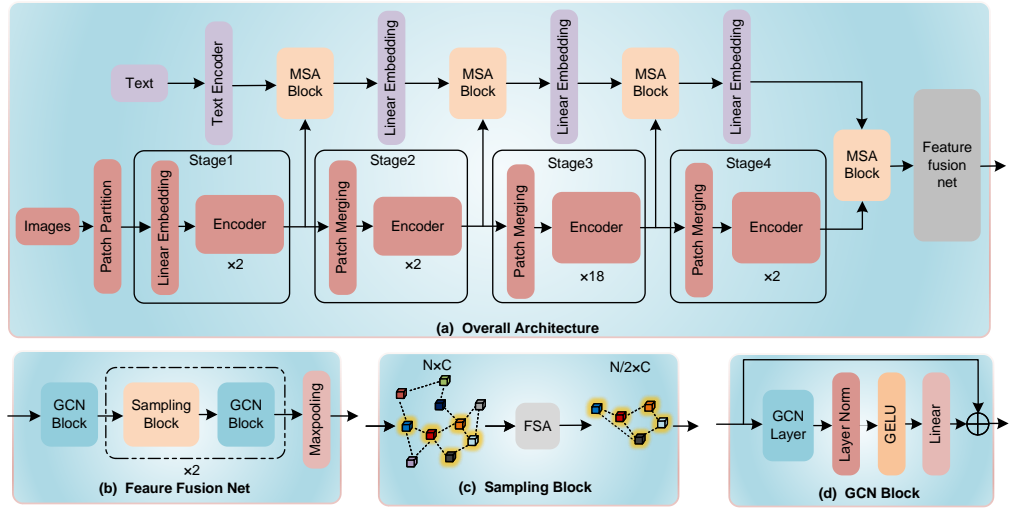


Figure 1. (a) The Overall architecture of HGT. (b) The architecture of GCN Feature Fusion Net. The Encoder in our architecture is a ViT based Encoder. (c) The Sampling Block using FSA Algorithm to sample from multiple features. (d) A GCN Block that maintains the dimensionality of input features and output features.

2. Related Work

2.1. PJI Diagnosis

Periprosthetic joint infection (PJI) diagnosis has been a topic of interest in recent years due to the increased prevalence of joint replacement surgeries. Various studies have focused on the development of new markers or the combination of existing markers to improve the specificity and sensitivity of PJI diagnosis [11][12][1]. Other research has investigated the use of imaging techniques, such as ultrasound [13], MRI [14], and nuclear imaging [14], to provide additional information on the infection status within the joint.

As a high robustness way, machine learning-based methods are capable of identifying personalized important features missing from criteria-based methods and providing interpretable decision support for individual diagnosis [15]. Klemt et al. have compared three different machine learning methods: Artificial Neural Network (ANN), Random Forest, Elastic-net Penalized Logistic Regression in PJI diagnosis [16]. Tao et al. use Convolutional Neural Network (CNN) to analyze the pathological sections of PJI patients under high magnification fields [17]. For greater accuracy, integrating information from different modality (clinical performance, biochemical test results, radiographical examinations) is highly important with imaging findings can potentially improve diagnostic accuracy. However, such diagnostic methods based on the fusion of multimodal information is still to be established.

2.2. Transformer

The transformer architecture, first introduced by Vaswani et al. [18], has become a cornerstone in the development of deep learning models for natural language processing and computer vision tasks. Transformer-based models have shown exceptional performance in a wide range of applications, including machine translation [18], text summarization [19], and image classification [20]. Specifically, ViT [20], SWIN [21], and Max-ViT [22] are transformer-based visual architectures that have shown great promise in feature extraction from images.

In disease diagnosis, transformer-based methods have shown its high practicality. Lei et al. developed an automated diagnosis framework of covid19 in chest CTs based on SWIN Transformer [23]. Jafari et al. use Deep Transformers and Explainable Artificial Intelligence for Automatic Diagnosis of Myocarditis Disease in Cardiac MRI Modality

[24]. Xu et al. have developed a Hierarchical Transformer for Eye Diseases Diagnosis [25]. Nogales et al. have applied BERT in Parkinson’s Disease diagnosis. In recent trends, Transformer-based multimodal architectures are widely used for high accurate diagnosis. Xing et al. propose a method for alzheimer disease diagnosis by fusing multimodal visual features using Transformer [26]. Dai et al. have developed a multimodal method for image classification using Transformer [27]. Cai et al. have developed a method for skin disease by fusing images and metadata using transformer [28]. As above, for PJI diagnosis, Transformer-based multimodal architectures can be a suitable candidates for improving diagnostic accuracy.

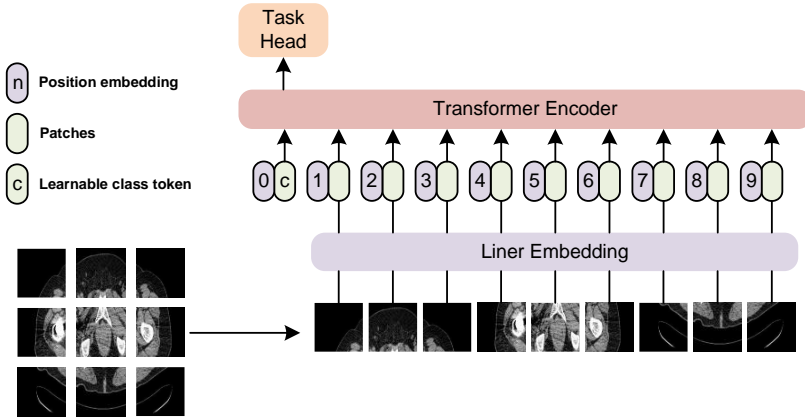


Figure 2. The general architecture of ViT based Transformer. We split an image into multiple patches, and feed them into the Transformer Encoder. A Task Head is incorporated at the end of the architecture.

2.3. GCN

Graph Convolutional Networks (GCNs) [10] are effective tools for analyzing graph-structured data. They have demonstrated success in diverse domains, such as, including social network analysis [29], drug discovery [30], and computer vision [31] and recommendation systems [32]. GCNs excel in handling irregular data structures and capturing the relational information between data points, making them an ideal choice for feature fusion.

Numerous applications exist for feature fusion based on Graph Convolutional Networks (GCNs). In semantic segmentation field, GCNs are used as a feature fusion tool during semantic segmentation process [33]. Apart from that, GCNs have also been used for feature fusion during hyperspectral image classification [34] [35]. For traffic prediction, GCNs are used to build traffic network flow for deep feature fusion [36]. As in medical feature integration, GCNs have also been widely used. The feature derived from different medical characteristics can be easily integrated to diagnosis versatile diseases [37] [38] [39]. Thus, the potential of GCNs in integrating large scale radiographical features can be easily shown.

In our work, we represent a CT images graph and define GCN on it. By a proposed feature sampling algorithm (FSA), our novel GCN based feature fusion network can easily achieve feature integration between numerous CT images with low parameters.

3. Methods

In our design, the proposed architecture processes multiple CT images and medical numerical vectors within a single feedforward calculation. All images belonging to a single CT scan initially undergo a Sampling Strategy to reduce computational complexity. Subsequently, the sampled images and medical numerical vectors are fed into the network for in-depth feature extraction and combination. Finally, the deeply fused features extracted

by the first four stages of the network are fed into a GCN Feature Fusion network to obtain the final fused feature, denoted as f_{out} . This feature is directly used for diagnosing periprosthetic joint infection (PJI).

3.1. Sampling Strategy

For two primary reasons, directly feeding all images from a single CT scan into our proposed architecture poses challenges: 1) a single CT scan generates hundreds of images, which could significantly increase computational complexity and training difficulty; 2) the number of images produced by a single CT scan varies, leading to an uneven distribution of images within the dataset.

To effectively address these issues, a sampling strategy is applied to each CT scan. An ideal sampling strategy should select an equal number of images from different CT scans while preserving the overall features of the original CT scans. A uniform sampling strategy maintains the number of sampled images but reduces the number of used images. Alongside feature reduction, this approach may substantially decrease the network's performance.

As a solution, a random distribution can be introduced on top of the uniform sampling method. Assuming the number of images generated by a single CT scan is N , with picture index $index_k, k \in 0, 1, \dots, N - 1$. The target number of sampled images is N_S . The images are divided into N_S non-overlapping groups, $S_i, i \in 0, 1, \dots, N_S - 1$, based on their index. During sampling, an image within group S_i is randomly chosen as the group's sampled image, denoted as n_i . The final image set can be represented as $n_0, n_1, \dots, n_{N_S - 1}$, as illustrated in Figure 3.

This method not only addresses the aforementioned issues but also allows all images in the original CT scan to be utilized by the network during training, as the sampled image sets differ each time.

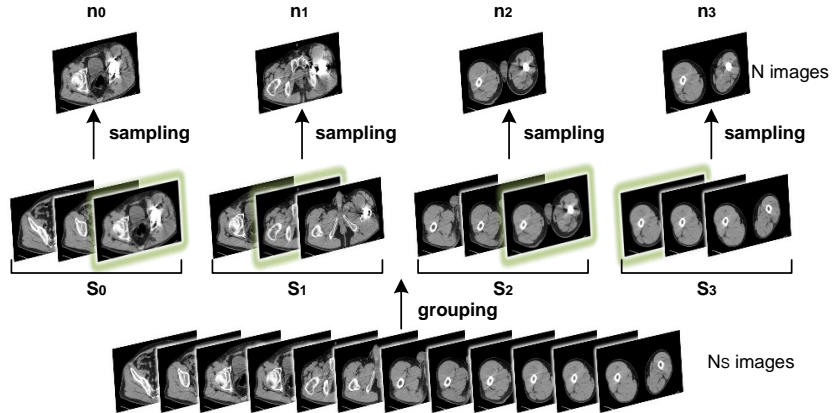


Figure 3. The process of sampling Strategy, with $N = 4$, $N_S = 12$ here for illustration

3.2. Unidirectional Selective Attention

In mainstream transformer-based multimodal architectures, Cross-Attention is widely employed for feature integration between vision and text modalities. The information flow between these two modalities in this attention mechanism is bidirectional. For PJI diagnosis, the vision modality consists of high-noise CT images, while patient text features comprise single numerical vectors that are considerably smaller in data volume compared to images and could exhibit a stronger correlation with PJI. Consequently, the difficulty of employing bidirectional Cross-Attention for cross-modal feature integration is apparent due to the overfitting of text data and neglect of image feature extraction. In contrast, the Unidirectional Selective Attention (USA) we propose can easily circumvent this issue.

In our Unidirectional Selective Attention (USA) mechanism, only a one-way information flow exists from vision to text modality. This mechanism allows the text to directly select key information from high-noise images for modality combination, accelerating the feature fusion between image and text information. Initially, text features are extracted by encoding the original text information $T \in R^{\text{dim}T}$ through a linear transformation Encoder. The resulting text feature, denoted as $F^T \in R^{\text{dim}T}$, can be represented as:

$$F^T = \text{Encoder}(T; \theta_{\text{Encoder}}) \quad (1)$$

where Encoder is a linear transformation with an output dimension of $\text{dim}T$. Subsequently, the input image feature $F^I \in R^{N \times \text{dim}}$ is considered, along with the Q, K, and V vectors of the attention mechanism. The Q, K, and V vectors can be expressed as:

$$Q = \Psi_1(F^T; \theta_{\Psi_1}) \quad (2)$$

$$K = \Psi_2([F^T, F_0^I, F_1^I, \dots, F_N^I]; \theta_{\Psi_2}) \quad V = \Psi_3([F^T, F_0^I, F_1^I, \dots, F_N^I]; \theta_{\Psi_3}) \quad (3)$$

In these expressions, $[\cdot]$ denotes the concatenation operation, and Ψ represents a linear transformation with parameters θ_{Ψ} . For practical purposes, a multi-head attention mechanism is employed. Thus, the Unidirectional Selective Attention (USA) can be represented as:

$$USA(Q, K, V) = \Psi_0[\text{head}_1, \dots, \text{head}_h] \quad (4)$$

$$\text{head}_i = \text{Attention}(\Psi_i^Q(Q), \Psi_i^K(K), \Psi_i^V(V)) \quad (5)$$

where the Attention is the same as in ViT [20], and $[\cdot]$ denotes the concatenation operation.

Through this mechanism, the low-noise information in the images can be selected by the text information for more efficient modality combination. In practice, the Unidirectional Selective Attention (USA) has been incorporated by utilizing the structure depicted in Figure 4.

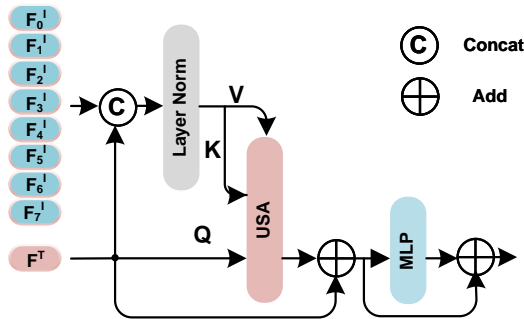


Figure 4. The detailed architecture of the Unidirectional Selective Attention Block. MLP here is a 2 layer Multilayer Perception with GeLU activate function [40], USA is the Unidirectional Selective Attention mechanism proposed above.

3.3. GCN Feature Fusion Net

After the first four stages of the entire architecture, the integrated features of text and images can be obtained, which can be denoted as $F^I \in R^{N \times \text{dim}}$. To further acquire a lower-dimensional feature representation, F^I is processed by the GCN Feature Fusion Net, as illustrated in Figure 5.

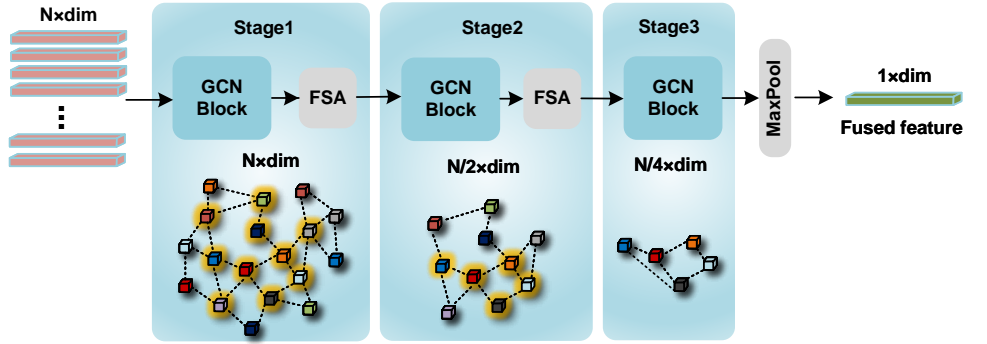


Figure 5. The detailed architecture of the GCN Feature Fusion Net. This intricate architecture encompasses three stages. Within each stage, the number of features progressively diminishes, with the feature count reducing by half following every FSA implementation.

3.4. Graph Based on Features of CT Images and Text

Upon obtaining the integrated features F^I , an undirected graph G with N nodes based on the vectors F^I can be constructed to represent the intrinsic relationships between multiple features. The adjacency matrix of this graph, $S \in R^{N \times N}$, is defined as follows:

$$S_{ij} = \Omega(g_{ij}; \theta_\Omega) \quad (6)$$

where $g_{ij} = [F_i^I, F_j^I, |F_i^I - F_j^I|^2] \in R^{2 \times \text{dim} + 1}$ represents the spatial relation of two distinct image features, and $[]$ denotes vectorized concatenation of elements. Ω is a three-layer MLP with GeLU activation function, and its parameters are denoted by θ_Ω , with the MLP outputting a scalar S_{ij} .

Next, the KNN algorithm is utilized, based on the index of the input images, to calculate the k nearest neighbors for each feature, retaining only the edges between neighboring features in G . Consequently, the sparse adjacency matrix A for G is obtained, defined as:

$$A_{ij} = S_{ij} \cdot \mathbb{I}\{F_j^I \in N(F_i^I)\} \quad (7)$$

where $\mathbb{I}(\cdot)$ is a binary function indicating whether F_j^I is the neighbor of F_i^I . Clearly, the undirected graph G effectively represents the abstract relationships between the features of each image, encompassing the complete image features and text features.

3.5. Image Feature Fusion and Sampling

The Graph Convolutional Neural Network (GCN) is well-suited for learning abstract relationships between nodes in an undirected graph and can learn the abstract representation of the entire graph. Let G^l represent the feature undirected graph at the l -th stage; a forward pass of the l -th stage GCN Block in our network can be defined as:

$$F_{\text{middle}}^l = \Gamma(A^l \text{LN}(F^l), \theta_\Gamma) W^l + F^l \quad (8)$$

where A^l represents the sparse adjacency matrix of G^l , LN represents Layer Normalization [41], $W^l \in R^{d \times d}$ is the learnable weight matrix, and $\Gamma(\cdot)$ is a non-linear transform comprising a Layer Normalization followed by a GeLU activation. The dimension of F^l remains the same before and after the GCN Blocks.

Next, in order to extract global features, the undirected graph G must be coarsened. Let the coarsened features be defined as F^{l+1} . Ideally, if the feature information remains unchanged before and after coarsening, the prediction results using the pre-coarsened features F_{middle}^l and the post-coarsened features F^{l+1} should be the same. As for PJI diagnosis, if any of the features F_i^l among F^l shows positive, the diagnosis should be considered positive.

The final diagnostic judgment largely depends on the most significant features among the many features in feature matrix F ; therefore, it is necessary to retain these features in the coarsened feature matrix F^{l+1} from F_{middle}^l . To meet the above requirements, a novel selective feature sampling strategy (FSA) based on the \max function has been designed. The FSA strategy can be defined as:

$$j = \arg \max_{i \leq N} \max(\Phi(F_{middle,i}^l, \theta\Phi)), M \quad (9)$$

$$F^{l+1} = F_{middle,j}^l \quad (10)$$

where N denotes the quantity of image features prior to sampling, and M signifies the number of image features after sampling has occurred. The term \max refers to the process of obtaining the highest value within a vector, and $\arg\max(\cdot)$ represents the extraction of index values corresponding to the top M largest elements present in the input vector. Φ is a two-layer MLP incorporating the GeLU activation function, and its parameters θ_Φ can be effectively trained utilizing the loss described in section 2.5 Network Training.

With this strategy, a coarsened graph G^{l+1} along with its new nodes F^{l+1} can be obtained. By stacking GCN Blocks and FSA, the architecture of GCN Feature Fusion Net can be achieved. After passing the features F^1 through the GCN Feature Fusion Net, the low-dimensional representation of fused feature can be obtained.

4. Implementation and Results

4.1. Datasets

In this study, a custom-built Periprosthetic Joint Infection (PJI) dataset is employed. The dataset includes 103,049 black and white image samples and 489 numerical text samples. Each text sample comprises 14 numerical indicators. All text samples are normalized to $[0, 1]$. The composition of PJI dataset is presented in Table 1, while the composition of a single numerical text sample is shown in Table 2.

Table 1. The composition of the custom-built PJI dataset

Modality	Positive Samples			Negative Samples			Total Samples
	train	test	valid	train	test	valid	
image	25303	5517	13222	42106	5365	11536	103049
text	98	20	50	168	20	50	489
Total Positive Samples				Total Negative Samples			
image	44042			59007			
text	221			268			

Table 2. The composition of a single text sample.

Data Type	CPR	ESR	Lesion Site	Sex	Age	Hypertension	Diabetes
Value Range	[0,120]	[0,120]	0 or 1	0 or 1	[0,100]	0 or 1	0 or 1
Data Type	Rheumatoid Arthritis	Anemia	Osteoporosis	Cerebral infarction	Hypoalbuminemia	Hypothyroidism	Liver Disease
Value Range	0 or 1	0 or 1	0 or 1	0 or 1	0 or 1	0 or 1	0 or 1

4.2. Training Loss and Implementation Details

Within the comprehensive training framework, the overall loss function encompasses both Diagnosis and Select loss components. The total loss can be expressed as follows:

$$\mathcal{L} = \mathcal{L}_{Diagnosis}(\mathcal{A}(f_{out}), y) + \sum_{l=0}^{L-1} \sum_{i \in j} \mathcal{L}_{Select}(\Phi(F_{middle,j}^l, \theta_\Phi), y) \quad (11)$$

In this equation, y denotes the true label of the diagnosis, while both $\mathcal{L}_{Diagnosis}$ and \mathcal{L}_{Select} represent cross-entropy loss. \mathcal{A} signifies a fully connected (FC) layers with output dimensions of 2.

The model is trained for 200 epochs using a batch size of 128 (64 images per text and 2 texts in total) on a single NVIDIA RTX 4090 GPU. The AdamW optimizer is employed [1], featuring a weight decay of 0.01. The learning rate is warmed up to 1e-4 in the first 5 epochs and decays to 1e-6 following a cosine schedule. Images are resized to a resolution of 224×224 , with augmentations such as RandomHorizontalFlip and RandomRotation applied. The text vector size is set to 1×14 . The k-value for the KNN algorithm in each GCN layer is set to 2, while the M-values for all sampling block structures are equal to $N/2$. To expedite the training process, the NVIDIA AMP Strategy is utilized.

4.3. Evaluation Metrics

The accuracy (ACC) is a widely used performance metric that quantifies the proportion of correct predictions made by a model relative to the total number of predictions. Mathematically, it can be expressed as:

$$ACC = \frac{TP + TN}{TP + TN + FP + FN} \quad (12)$$

where TP is the number of true positives, TN is the number of true negatives, FP is the number of false positives, and FN is the number of false negatives.

The Area Under the Curve (AUC) is a performance metric that evaluates the trade-off between the true positive rate (sensitivity or recall) and the false positive rate (1 - specificity) at various threshold settings. Specifically, it refers to the area under the Receiver Operating Characteristic (ROC) curve. The true positive rate (TPR) and false positive rate (FPR) can be defined as follows:

$$TPR = \frac{TP}{TP + FN} \quad (13)$$

$$FPR = \frac{FP}{FP + TN} \quad (14)$$

Throughput, measured in images per second (images/s), is a performance metric commonly used to evaluate the efficiency of a machine learning model, particularly in the context of image processing and computer vision tasks. In our study, the Throughput of the model can be calculated through the following equation:

$$Throughput = \frac{N_I}{T_B \times B} \quad (15)$$

where N_I is the total number of processed images, T_B is the total processing time of one batch in seconds, and B represents Batchsize

4.4. Experiment On PJI Dataset

To evaluate the model's performance, experiments were conducted on the PJI dataset using various multimodal methods. The performance comparisons, based on the aforementioned settings, are presented in Table 3.

Under the basic settings, the HGT model significantly outperforms the most recent robust models. With only 68M parameters, HGT achieves a top-1 accuracy of 91.4% and an AUC of 0.959, surpassing the most powerful model by 2.9% in top-1 accuracy and 2.2% in AUC, while utilizing fewer parameters. In summary, the proposed model outperforms other models employing MLP, Merged-attention, and Co-attention as their Multimodal Fusion methods. The substantial improvement of our proposed model demonstrates the considerable advantage of using the USA and GCN Fusion Network as Multimodal Fusion methods for PJI diagnosis.

Table 3. Performance comparison under PJI dataset settings. Throughput is measured on a single RTX4090 GPU with batch size 128. In vision modality networks, text information obtained from the text encoder is processed through a three-layer Multi-layer Perception (MLP) featuring a GELU activation function, while the images are passed through the entire network accompanied by a Maxpool operation in the batch dimension. The fused image and text features are directly concatenated to perform PJI prediction

Model	Eval size	Multimodal Fusion	Parameters	Throughput (image/s)	ACC	AUC
SWIN-B[21]	224 ²		88M	483	88.5	92.6
ViT-B[20]	224 ²	MLP	86M	630	85.3	91.5
MaxViT-S[22]	224 ²		79M	428	87.3	93.7
ViLT[6]	224 ²	Merged-attn.	88M	624	87.0	93.7
UniT[9]	224 ²		135M	556	81.7	91.2
BLIP[42]	224 ²	Cross-attn.	147M	549	85.8	93.1
ALBEF[43]	224 ²		149M	547	85.5	93.2
HGT	224 ²	USA+GCN	68M	552	91.4	95.9

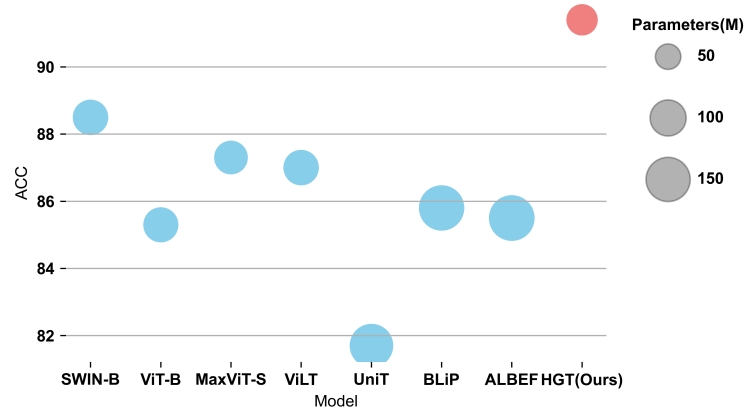


Figure 6. The ACC of different models under the same experiment configuration.

4.5. Ablation Study

To assess the effectiveness of the USA Block and GCN Feature Fusion Network, an ablation study was conducted. The results are presented in Table 4. As illustrated, the USA Block methods considerably outperform the Non-USA Block methods, yielding an increase of up to 3.5% in top-1 accuracy and 5.6% in AUC. Furthermore, the GCN Feature Fusion Network methods exhibit significant improvement over the Non-Fusion Network methods, with gains of up to 2.4% in top-1 accuracy and 3.6% in AUC.

Table 4. The ablation study results are presented. In the Non-USA Block methods, text information acquired from the text encoder undergoes processing through a three-layer Multilayer Perceptron (MLP) with a GELU activation function, while images pass through the entire SWIN-S network, followed by a Maxpool operation in the batch dimension. The fused image and text features are directly concatenated for PJI prediction. In the Non-Fusion Network methods, the GCN Feature Fusion Network is substituted with an Averagepool operation.

Feature Fusion Method	ACC	AUC
<i>Avg</i>	87.9	90.3
<i>GCN</i>	90.3	93.9
<i>USA + Avg</i>	90.0	92.9
<i>USA + GCN</i>	91.4	95.9

¹ Tables may have a footer.

In order to examine the implications of each block, Gradient Class Activation Mapping++ (Grad-CAM++) [44] was employed on a single PJI-positive CT scan to visualize the features extracted by different models. Sixteen uniformly sampled images from the same CT examination were input into the network, with the results displayed in Figure 7. It is evident that the GCN feature fusion network enhances performance by enabling a heightened focus on images related to the lesion site. Additionally, incorporating the USA Block facilitates more precise identification of regions within images where the infection occurs.

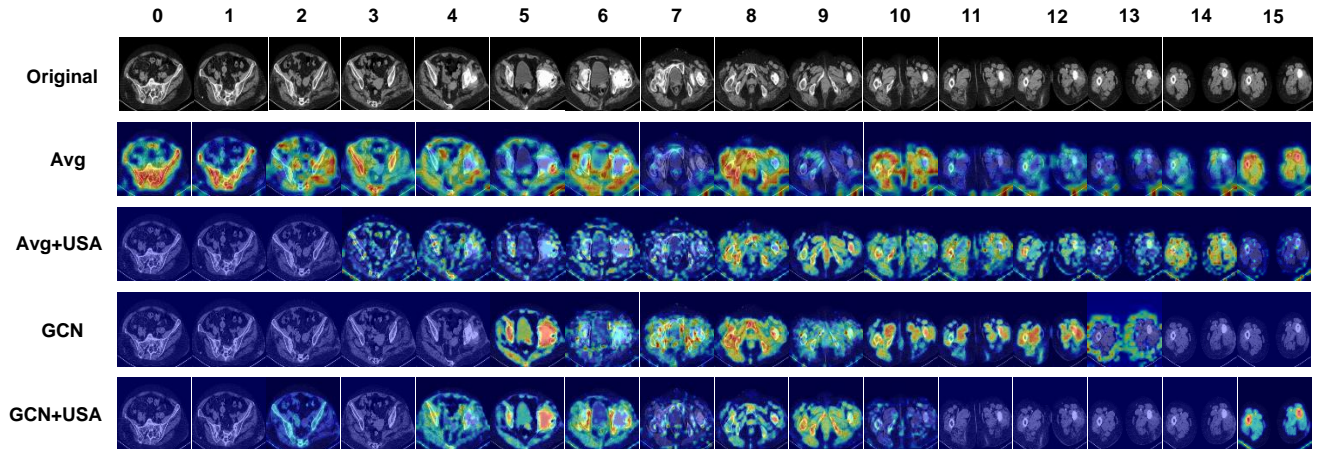


Figure 7. The visualization results of the methods based on ablation study settings are presented. In the Figure, "Avg" represents the Averagepool, USA represents the Unidirectional Selective Attention, while "GCN" denotes the GCN Feature FuseNet. The images with index ranging from 4 to 8 are observed to contain features indicative of infection occurrence, with the infection manifesting in the patient's right hip bone.

4.5.1. Influence of k in Undirected Graph Construction

The value of k , an important hyperparameter in the KNN algorithm for GCN Undirected Graph Construction, is tested for various values to assess model performance. The feature maps are visualized using Grad-CAM++ to evaluate the feature extraction capabilities.

Table 5. Performance with different k values.

k	Feature Fusion Method	ACC	AUC
2	USA + GCN	91.4	95.9
4	USA + GCN	90.6	94.1
6	USA + GCN	89.4	92.4

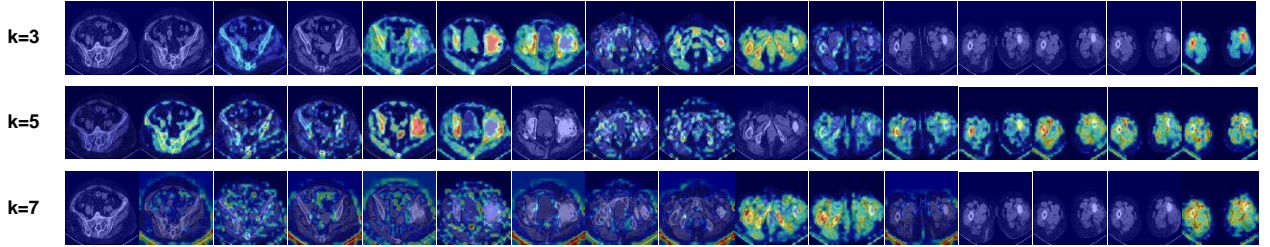


Figure 8. Visualization results of methods based on different k values. The original images are the same as in Figure 7

Model performance results are presented in Table 5. It is evident that performance declines as the value of k increases. The k=2 model outperforms the k=4 model by 0.8% in ACC and 1.8% in AUC. The k=4 model shows a 1.2% higher ACC and a 1.7% higher AUC compared to the k=6 model.

To explain these results, the visualization outcomes are displayed in Figure 8. The ability to locate lesion sites in all CT images and focus on a single lesion within an image diminishes with increasing k values. As k increases, the GCN can aggregate more non-neighborhood features, resulting in a dilution of local features and, consequently, reduced model performance.

4.5.2. Impact of Sampling Strategy

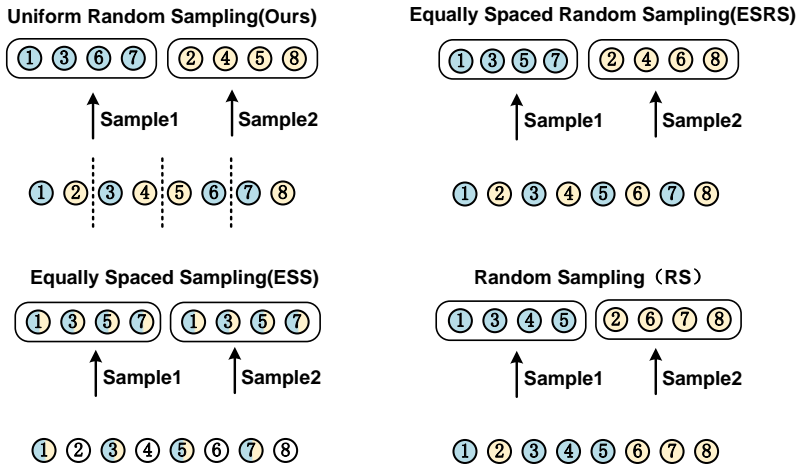


Figure 9. This figure illustrates the detailed mechanisms of four different sampling strategies, where two batches of images are obtained from the same CT scan using four distinct approaches.

The choice of sampling strategies can significantly impact a model's performance. Various sampling strategies are evaluated using the same settings as the experiment on the

PJI dataset, as depicted in Figure 9. The feature extraction capabilities of these strategies are assessed by visualizing the feature maps using Grad-CAM++.

Table 6. Performance with different Sampling Strategies.

Sample Strategy	Uniform Random Sampling(Ours)	Equally Spaced Random Sampling(ESRS)	Equally Spaced Sampling(ESS)	Random Sampling(RS)
ACC	91.4	90.9	88.5	89.4
AUC	95.9	92.8	92.3	93.4

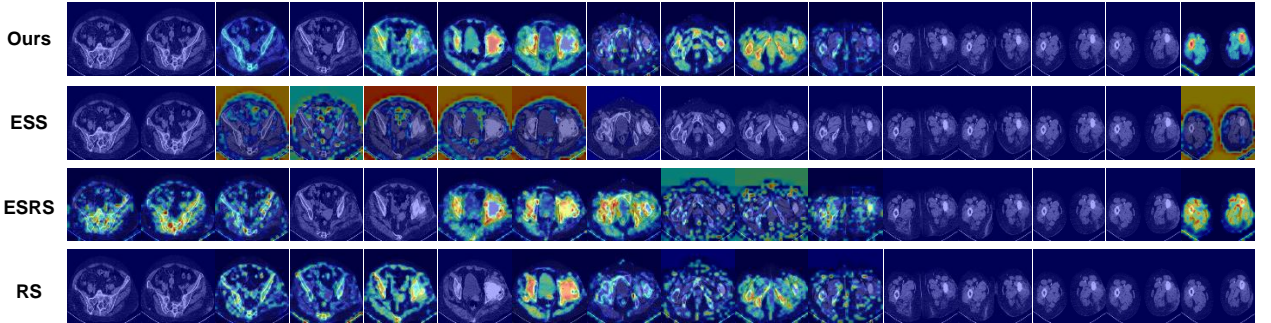


Figure 10. Visualization results of methods based on different Sampling Strategies. The original images are the same as in Figure 7

The model performance results are displayed in Table 6. As observed, our sampling strategy outperforms other strategies. Our sampling strategy bring a promotion in both ACC and AUC by 2.9% and 3.6%, respectively, when compared to the least effective sampling strategy. The suboptimal performance of the Equally Spaced Sampling Strategy can be ascribed to the diminished number of CT image samples. The Equally Spaced Random Sampling Strategy surpasses the Equally Spaced Sampling Strategy by 2.4% in ACC and 0.5% in AUC, which can be attributed to the comprehensive utilization of the CT image dataset. The Random Sampling Strategy results in a performance decline due to the increased difficulty for the GCN Feature Fusion network in learning the topological structures of the undirected graph. The shortcomings of other sampling strategies further underscore the efficacy of our sampling strategy.

The aforementioned analysis is corroborated by the visualization results in Figure 10. Among all strategies, our approach attains the highest concentration on lesion sites.

5. Conclusions

In conclusion, this study introduces a Hierarchical CGN-Based Transformer: HGT for multimodal PJI diagnosis, utilizing CT images and patients' numerical text data to enhance diagnostic accuracy. A distinctive sampling strategy was implemented, along with a GCN-based feature fusion approach for efficient image processing and precise infection localization. Moreover, an Unidirectional Selective Attention (USA) Block was employed to balance learning between easily acquired low-noise text and challenging high-noise image modalities.

The proposed method was validated using a custom-built PJI dataset and compared to multiple competitive multimodal methods under the same experimental configuration. The results demonstrate that the ACC of this method reaches 91.4%, which is 2.9% higher than the most recent powerful model, and the AUC attains 95.9%, signifying a substantial improvement of 2.2% compared to other methods with fewer parameters.

In the future, we aim to expand this approach to other complications, harnessing the power of large-scale language generation models to achieve automatic diagnosis and case writing for multiple concurrent conditions.

Author Contributions: R.L.: writing, theoretical framework, methodology. F.Y.: data curation, resources, review and editing. X.L.: review and editing, methodology. H.S.: review and editing. All authors have read and agreed to the published version of the manuscript.

Funding: Sichuan Provincial student Innovation and Entrepreneurship Funding: C2023125222

Data Availability Statement: Due to privacy restrictions, the dataset has not been published yet. You can contact the corresponding author to obtain.

Conflicts of Interest: The authors declare no conflict of interest.

References

1. Parvizi, J.; Tan, T.L.; Goswami, K.; Higuera, C.; Della Valle, C.; Chen, A.F.; Shohat, N. The 2018 definition of periprosthetic hip and knee infection: an evidence-based and validated criteria. *The Journal of arthroplasty* **2018**, *33*, 1309–1314.
2. Signore, A.; Sconfienza, L.M.; Borens, O.; Glaudemans, A.W.; Cassar-Pullicino, V.; Trampuz, A.; Winkler, H.; Gheysens, O.; Vanhoenacker, F.M.; Petrosillo, N.; et al. Consensus document for the diagnosis of prosthetic joint infections: a joint paper by the EANM, EBJIS, and ESR (with ESCMID endorsement). *European journal of nuclear medicine and molecular imaging* **2019**, *46*, 971–988.
3. Falstie-Jensen, T.; Lange, J.; Daugaard, H.; Vendelbo, M.; Sørensen, A.; Zerahn, B.; Ovesen, J.; Søballe, K.; Gormsen, L.; study-group BS Olsen HVS Johanssen B. Elmengaard TM Thillemann L. Bolvig, R. 18F FDG-PET/CT has poor diagnostic accuracy in diagnosing shoulder PJI. *European Journal of Nuclear Medicine and Molecular Imaging* **2019**, *46*, 2013–2022.
4. Fayad, L.M.; Carrino, J.A.; Fishman, E.K. Musculoskeletal infection: role of CT in the emergency department. *Radiographics* **2007**, *27*, 1723–1736.
5. Baltrušaitis, T.; Ahuja, C.; Morency, L.P. Multimodal machine learning: A survey and taxonomy. *IEEE transactions on pattern analysis and machine intelligence* **2018**, *41*, 423–443.
6. Kim, W.; Son, B.; Kim, I. Vilt: Vision-and-language transformer without convolution or region supervision. In Proceedings of the International Conference on Machine Learning. PMLR, 2021, pp. 5583–5594.
7. Lu, J.; Batra, D.; Parikh, D.; Lee, S. Vilbert: Pretraining task-agnostic visiolinguistic representations for vision-and-language tasks. *Advances in neural information processing systems* **2019**, *32*.
8. Qi, D.; Su, L.; Song, J.; Cui, E.; Bharti, T.; Sacheti, A. Imagebert: Cross-modal pre-training with large-scale weak-supervised image-text data. *arXiv preprint arXiv:2001.07966* **2020**.
9. Hu, R.; Singh, A. Unit: Multimodal multitask learning with a unified transformer. In Proceedings of the Proceedings of the IEEE/CVF International Conference on Computer Vision, 2021, pp. 1439–1449.
10. Kipf, T.N.; Welling, M. Semi-supervised classification with graph convolutional networks. *arXiv preprint arXiv:1609.02907* **2016**.
11. Ghanem, E.; Antoci Jr, V.; Pulido, L.; Joshi, A.; Hozack, W.; Parvizi, J. The use of receiver operating characteristics analysis in determining erythrocyte sedimentation rate and C-reactive protein levels in diagnosing periprosthetic infection prior to revision total hip arthroplasty. *International Journal of Infectious Diseases* **2009**, *13*, e444–e449.
12. Parvizi, J.; Zmistowski, B.; Berbari, E.F.; Bauer, T.W.; Springer, B.D.; Della Valle, C.J.; Garvin, K.L.; Mont, M.A.; Wongworawat, M.D.; Zalavras, C.G. New definition for periprosthetic joint infection: from the Workgroup of the Musculoskeletal Infection Society. *Clinical Orthopaedics and Related Research®* **2011**, *469*, 2992–2994.
13. Randelli, F.; Brioschi, M.; Randelli, P.; Ambrogi, F.; Sdao, S.; Aliprandi, A. Fluoroscopy-vs ultrasound-guided aspiration techniques in the management of periprosthetic joint infection: which is the best? *La radiologia medica* **2018**, *123*, 28–35.
14. Love, C.; Marwin, S.E.; Palestro, C.J. Nuclear medicine and the infected joint replacement. In Proceedings of the Seminars in nuclear medicine. Elsevier, 2009, Vol. 39, pp. 66–78.
15. Kuo, F.C.; Hu, W.H.; Hu, Y.J. Periprosthetic Joint Infection Prediction via Machine Learning: Comprehensible Personalized Decision Support for Diagnosis. *The Journal of Arthroplasty* **2022**, *37*, 132–141. <https://doi.org/https://doi.org/10.1016/j.arth.2021.09.005>.
16. Klemt, C.; Laurencin, S.; Uzosike, A.C.; Burns, J.C.; Costales, T.G.; Yeo, I.; Habibi, Y.; Kwon, Y.M. Machine learning models accurately predict recurrent infection following revision total knee arthroplasty for periprosthetic joint infection. *Knee Surgery, Sports Traumatology, Arthroscopy* **2021**, pp. 1–9.
17. Tao, Y.; Hu, H.; Li, J.; Li, M.; Zheng, Q.; Zhang, G.; Ni, M. A preliminary study on the application of deep learning methods based on convolutional network to the pathological diagnosis of PJI. *Arthroplasty* **2022**, *4*, 49.
18. Vaswani, A.; Shazeer, N.; Parmar, N.; Uszkoreit, J.; Jones, L.; Gomez, A.N.; Kaiser, L.; Polosukhin, I. Attention is all you need. *Advances in neural information processing systems* **2017**, *30*.
19. Liu, Y. Fine-tune BERT for extractive summarization. *arXiv preprint arXiv:1903.10318* **2019**.
20. Dosovitskiy, A.; Beyer, L.; Kolesnikov, A.; Weissenborn, D.; Zhai, X.; Unterthiner, T.; Dehghani, M.; Minderer, M.; Heigold, G.; Gelly, S.; et al. An image is worth 16x16 words: Transformers for image recognition at scale. *arXiv preprint arXiv:2010.11929* **2020**.

21. Liu, Z.; Lin, Y.; Cao, Y.; Hu, H.; Wei, Y.; Zhang, Z.; Lin, S.; Guo, B. Swin transformer: Hierarchical vision transformer using shifted windows. In Proceedings of the Proceedings of the IEEE/CVF international conference on computer vision, 2021, pp. 10012–10022.
22. Tu, Z.; Talebi, H.; Zhang, H.; Yang, F.; Milanfar, P.; Bovik, A.; Li, Y. Maxvit: Multi-axis vision transformer. In Proceedings of the Computer Vision–ECCV 2022: 17th European Conference, Tel Aviv, Israel, October 23–27, 2022, Proceedings, Part XXIV. Springer, 2022, pp. 459–479.
23. Zhang, L.; Wen, Y. A transformer-based framework for automatic COVID19 diagnosis in chest CTs. In Proceedings of the Proceedings of the IEEE/CVF International Conference on Computer Vision, 2021, pp. 513–518.
24. Jafari, M.; Shoeibi, A.; Ghassemi, N.; Heras, J.; Khosravi, A.; Ling, S.H.; Alizadehsani, R.; Beheshti, A.; Zhang, Y.D.; Wang, S.H.; et al. Automatic Diagnosis of Myocarditis Disease in Cardiac MRI Modality using Deep Transformers and Explainable Artificial Intelligence. *arXiv preprint arXiv:2210.14611* **2022**.
25. Ye, X.; Xiao, M.; Ning, Z.; Dai, W.; Cui, W.; Du, Y.; Zhou, Y. NEEDED: Introducing Hierarchical Transformer to Eye Diseases Diagnosis. In Proceedings of the Proceedings of the 2023 SIAM International Conference on Data Mining (SDM). SIAM, 2023, pp. 667–675.
26. Xing, X.; Liang, G.; Zhang, Y.; Khanal, S.; Lin, A.L.; Jacobs, N. Advit: Vision transformer on multi-modality pet images for alzheimer disease diagnosis. In Proceedings of the 2022 IEEE 19th International Symposium on Biomedical Imaging (ISBI). IEEE, 2022, pp. 1–4.
27. Dai, Y.; Gao, Y.; Liu, F. Transmed: Transformers advance multi-modal medical image classification. *Diagnostics* **2021**, *11*, 1384.
28. Cai, G.; Zhu, Y.; Wu, Y.; Jiang, X.; Ye, J.; Yang, D. A multimodal transformer to fuse images and metadata for skin disease classification. *The Visual Computer* **2022**, pp. 1–13.
29. Hamilton, W.; Ying, Z.; Leskovec, J. Inductive representation learning on large graphs. *Advances in neural information processing systems* **2017**, *30*.
30. Duvenaud, D.K.; Maclaurin, D.; Iparraguirre, J.; Bombarell, R.; Hirzel, T.; Aspuru-Guzik, A.; Adams, R.P. Convolutional networks on graphs for learning molecular fingerprints. *Advances in neural information processing systems* **2015**, *28*.
31. Wang, Y.; Sun, Y.; Liu, Z.; Sarma, S.E.; Bronstein, M.M.; Solomon, J.M. Dynamic graph cnn for learning on point clouds. *AcM Transactions On Graphics (tog)* **2019**, *38*, 1–12.
32. Ying, R.; He, R.; Chen, K.; Eksombatchai, P.; Hamilton, W.L.; Leskovec, J. Graph convolutional neural networks for web-scale recommender systems. In Proceedings of the Proceedings of the 24th ACM SIGKDD international conference on knowledge discovery & data mining, 2018, pp. 974–983.
33. Zhang, Z.; Zhang, X.; Peng, C.; Xue, X.; Sun, J. Exfuse: Enhancing feature fusion for semantic segmentation. In Proceedings of the Proceedings of the European conference on computer vision (ECCV), 2018, pp. 269–284.
34. Liu, Q.; Xiao, L.; Yang, J.; Wei, Z. CNN-enhanced graph convolutional network with pixel-and superpixel-level feature fusion for hyperspectral image classification. *IEEE Transactions on Geoscience and Remote Sensing* **2020**, *59*, 8657–8671.
35. Ding, Y.; Zhang, Z.; Zhao, X.; Hong, D.; Cai, W.; Yu, C.; Yang, N.; Cai, W. Multi-feature fusion: graph neural network and CNN combining for hyperspectral image classification. *Neurocomputing* **2022**, *501*, 246–257.
36. Li, Z.; Xiong, G.; Tian, Y.; Lv, Y.; Chen, Y.; Hui, P.; Su, X. A multi-stream feature fusion approach for traffic prediction. *IEEE transactions on intelligent transportation systems* **2020**, *23*, 1456–1466.
37. Wang, S.H.; Govindaraj, V.V.; Górriz, J.M.; Zhang, X.; Zhang, Y.D. Covid-19 classification by FGCNet with deep feature fusion from graph convolutional network and convolutional neural network. *Information Fusion* **2021**, *67*, 208–229.
38. Zhang, Q.; Zhou, J.; Zhang, B. Graph based multichannel feature fusion for wrist pulse diagnosis. *IEEE Journal of Biomedical and Health Informatics* **2020**, *25*, 3732–3743.
39. Song, X.; Zhou, F.; Frangi, A.F.; Cao, J.; Xiao, X.; Lei, Y.; Wang, T.; Lei, B. Multi-center and multi-channel pooling GCN for early AD diagnosis based on dual-modality fused brain network. *IEEE Transactions on Medical Imaging* **2022**.
40. Gardner, M.W.; Dorling, S. Artificial neural networks (the multilayer perceptron)—a review of applications in the atmospheric sciences. *Atmospheric environment* **1998**, *32*, 2627–2636.
41. Ba, J.L.; Kiros, J.R.; Hinton, G.E. Layer normalization. *arXiv preprint arXiv:1607.06450* **2016**.
42. Li, J.; Li, D.; Xiong, C.; Hoi, S. Blip: Bootstrapping language-image pre-training for unified vision-language understanding and generation. In Proceedings of the International Conference on Machine Learning. PMLR, 2022, pp. 12888–12900.
43. Li, J.; Selvaraju, R.; Gotmare, A.; Joty, S.; Xiong, C.; Hoi, S.C.H. Align before fuse: Vision and language representation learning with momentum distillation. *Advances in neural information processing systems* **2021**, *34*, 9694–9705.
44. Chattopadhyay, A.; Sarkar, A.; Howlader, P.; Balasubramanian, V.N. Grad-cam++: Generalized gradient-based visual explanations for deep convolutional networks. In Proceedings of the 2018 IEEE winter conference on applications of computer vision (WACV). IEEE, 2018, pp. 839–847.
45. Brigden, M.L. Clinical utility of the erythrocyte sedimentation rate. *American family physician* **1999**, *60*, 1443–1450.
46. Zmistowski, B.; Restrepo, C.; Huang, R.; Hozack, W.J.; Parvizi, J. Periprosthetic joint infection diagnosis: a complete understanding of white blood cell count and differential. *The Journal of arthroplasty* **2012**, *27*, 1589–1593.
47. Touvron, H.; Cord, M.; Douze, M.; Massa, F.; Sablayrolles, A.; Jégou, H. Training data-efficient image transformers & distillation through attention. In Proceedings of the International conference on machine learning. PMLR, 2021, pp. 10347–10357.

48. Squire, M.W.; Valle, C.J.D.; Parvizi, J. Preoperative diagnosis of periprosthetic joint infection: role of aspiration. *American Journal of Roentgenology* **2011**, *196*, 875–879.
49. Baltrušaitis, T.; Ahuja, C.; Morency, L.P. Multimodal machine learning: A survey and taxonomy. *IEEE transactions on pattern analysis and machine intelligence* **2018**, *41*, 423–443.
50. Show, A. Tell: Neural Image Caption Generation with Visual Attention Kelvin Xu. *Jimmy Ba, Ryan Kiros, Kyunghyun Cho, Aaron Courville, Ruslan Salakhutdinov, Richard Zemel, Yoshua Bengio arXiv* (2015-02-10) <https://arxiv.org/abs/1502.03044v3>.
51. Antol, S.; Agrawal, A.; Lu, J.; Mitchell, M.; Batra, D.; Zitnick, C.L.; Parikh, D. Vqa: Visual question answering. In Proceedings of the Proceedings of the IEEE international conference on computer vision, 2015, pp. 2425–2433.
52. Loshchilov, I.; Hutter, F. Fixing weight decay regularization in adam **2017**.